Showcasing research from the joint collaboration of Hae Jung Son's laboratory, Photo-electronic Hybrids Research Center, Korea Institute of Science and Technology (KIST) and Dae Sung Chung's laboratory, Chemical Engineering Chung-Ang University, Seoul, South Korea.

Enhancement of charge transport properties of small molecule semiconductors by controlling fluorine substitution and effects on photovoltaic properties of organic solar cells and perovskite solar cells

We developed a series of small molecule semiconductors and demonstrated that symmetricity and numbers of fluorine substitution of the molecule importantly affect its optical and morphological properties in a film. The molecule featured symmetric and even-numbered fluorine substitution patterns, displays improved molecular packing structures and higher crystalline properties in a film and thus, it achieved the high OTFT mobility and photovoltaic performance in both of organic solar cells and perovskite solar cells. It is demonstrated that low variation in the local dipole moment and the narrow distribution of molecular conformers make intermolecular interactions favorable, which may effectively drive crystal formations in the solid state and thus, higher charge transport properties.

As featured in:

See Dae Sung Chung,
Hae Jung Son *et al.*,
Chem. Sci., 2016, **7**, 6649.

ROYAL SOCIETY
OF **CHEMISTRY**

www.rsc.org/chemicalscience

Enhancement of charge transport properties of small molecule semiconductors by controlling fluorine substitution and effects on photovoltaic properties of organic solar cells and perovskite solar cells†

Jae Hoon Yun,[ac] Sungmin Park,[ad] Jin Hyuck Heo,[e] Hyo-Sang Lee,[af] Seongwon Yoon,[b] Jinback Kang,[g] Sang Hyuk Im,[e] Hyunjung Kim,[g] Wonmok Lee,[h] BongSoo Kim,[ai] Min Jae Ko,[aj] Dae Sung Chung*[b] and Hae Jung Son*[acf]

We prepared a series of small molecules based on 7,7′-(4,4-bis(2-ethylhexyl)-4*H*-silolo[3,2-*b*:4,5-*b*′]dithiophene-2,6-diyl)bis(4-(5′-hexyl-[2,2′-bithiophene]-5-yl)benzo[*c*][1,2,5]thiadiazole) with different fluorine substitution patterns (**0F**–**4F**). Depending on symmetricity and numbers of fluorine atoms incorporated in the benzo[*c*][1,2,5]thiadiazole unit, they show very different optical and morphological properties in a film. **2F** and **4F**, which featured symmetric and even-numbered fluorine substitution patterns, display improved molecular packing structures and higher crystalline properties in a film compared with **1F** and **3F** and thus, **2F** achieved the highest OTFT mobility, which is followed by **4F**. In the bulk heterojunction solar cell fabricated with PC$_{71}$BM, **2F** achieves the highest photovoltaic performance with an 8.14% efficiency and **0F** shows the lowest efficiency of 1.28%. Moreover, the planar-type perovskite solar cell (PSC) prepared with **2F** as a dopant-free hole transport material shows a high power conversion efficiency of 14.5% due to its high charge transporting properties, which were significantly improved compared with the corresponding PSC device obtained from **0F** (8.5%). From the studies, it is demonstrated that low variation in the local dipole moment and the narrow distribution of **2F** conformers make intermolecular interactions favorable, which may effectively drive crystal formations in the solid state and thus, higher charge transport properties compared with **1F** and **3F**.

1. Introduction

Organic conjugated materials have been extensively investigated for applications in a variety of optoelectronic devices, such as light-emitting diodes (OLEDs), field-effect transistors (OFETs), photovoltaic cells (OPVs), sensors, optical amplifiers, and lasers.[1–9] One key attraction of organic conjugated materials is the tunability of their physical and chemical properties through modifications of their molecular structures.[10–13] Their use in place of conventional inorganic semiconductors offers opportunities to reduce manufacturing costs by implementing printing technologies involving solution-processable materials that are capable of covering large areas and compatible with flexible substrates.[14–19]

Small molecule semiconductors have attracted significant research interest due to their advantages over polymeric semi-conductors. Small molecule semiconductors provide well-defined structures, a high purity, a high degree of order, and reduced batch-to-batch variation.[20] A representative application of small molecule semiconductors is their use as the electron-donating components in organic photovoltaic (OPV) devices. When blended with fullerene derivatives as electron acceptors, these materials can form a bulk heterojunction (BHJ) structure. The performances of solution-processed small-molecule-based BHJ OPVs (SM-OPVs) have steadily improved over the past several years, with power conversion efficiency (PCE) values in

^{a}Photoelectronic Hybrid Research Center, Korea Institute of Science and Technology, Seoul 02792, Republic of Korea. E-mail: hjson@kist.re.kr

^{b}School of Chemical Engineering and Material Science, Chung-Ang University, Seoul 06974, Republic of Korea. E-mail: dchung@cau.ac.kr

^{c}University of Science and Technology (UST), Daejeon 34113, Republic of Korea

^{d}Department of Chemistry, Korea University, Seoul 06974, Republic of Korea

^{e}Functional Crystallization Center (FCC), Department of Chemical Engineering, Kyung Hee University, Yongin-si 17104, Gyeonggi-do, Republic of Korea

^{f}Green School (School of Energy and Environment), Korea University, Seoul 02792, Republic of Korea

^{g}Department of Physics, Sogang University, Seoul 04107, Republic of Korea

^{h}Department of Chemistry, Sejong University, Seoul 05006, Republic of Korea

^{i}Department of Science Education, Ewha Womans University, Seoul, 03760, Republic of Korea

^{j}KU-KIST Graduate School of Converging Science and Technology, Korea University, Republic of Korea

† Electronic supplementary information (ESI) available: Experimental details including synthesis and experimental method. See DOI: 10.1039/c6sc02448c

excess of 10% in single-layer BHJ solar cells.[21] The notable performance enhancements are mostly attributed to the development of high-efficiency low-bandgap materials with a high charge carrier mobility.[21–23] Small molecule semiconductors also show promise for their utility in organic field effect transistors (OFETs), which require well-ordered semiconductor channels. Unlike polymeric semiconductors, the low molecular weight of a small molecule semiconductor enables fine structural/morphological tuning, so that preferential molecular arrangements may be efficiently formed.[24–26] The charge carrier mobilities of solution-processed small molecule semiconductors have improved continuously and now approach the mobilities of polymeric semiconductors.[27–29]

One effective synthetic strategy for achieving a low energy bandgap that simultaneously provides a good charge carrier mobility involves incorporating molecular electron donor (D) and acceptor (A) units in an alternating conjugated arrangement.[30,31] The resulting push–pull effects along the molecular backbone facilitate intramolecular charge transfer, resulting in an electronically delocalized structure.[32–34] This type of D–A small molecule material often exhibits a high hole mobility and good conductivity with potential utility as a dopant-free hole transport material (HTM) in efficient perovskite solar cells (PSCs), which have recently emerged as promising photovoltaic devices.[35–38] Therefore, the rational molecular design of D–A structures has given rise to high-performance materials with physical properties that are appropriate for use in SM-OPVs as well as in PSCs. Thus far, a range of material designs have been presented and synthetic efforts have been applied toward controlling the optical, electrical and solid state assembly properties of a material by varying the D and A subunits to have different electron donating and accepting abilities. Thiophene-based fused aromatic building blocks, such as 4H-silolo[3,2-b:4,5-b']dithiophene (DTS), benzo[1,2-b:4,5-b']dithiophene (BDT), and oligothiophene derivatives, have emerged as attractive D units, and electron-deficient compounds of benzo[c][1,2,5]thiadiazole (BT) and 2-(1,1-dicyanomethylene)rhodanine have been used effectively as A units in high-performance SM-OPVs.[39–42] A detailed understanding of the structure–property–function relationships within conjugated molecular materials has lagged behind the improvements in material design. It is particularly important to study the impacts of anchoring specific functional groups to a conjugated framework on the essential electrical properties, such as the charge carrier mobility. For example, the local dipole moment and electronic structures induced by functional groups can affect the intermolecular interactions and thus, the packing structures in a thin film.[43–45]

Herein, we prepared a series of conjugated molecules based on 7,7'-(4,4-bis(2-ethylhexyl)-4H-silolo[3,2-b:4,5-b']dithiophene-2,6-diyl)bis(4-(5'-hexyl-[2,2'-bithiophene]-5-yl)benzo[c][1,2,5]thiadiazole) (DTS(BTTh$_2$)$_2$) that incorporate different numbers of fluorine atoms on the BT unit. Difluoro-substituted DTS(FBTTh$_2$)$_2$ compounds are used in high-performance solution-processed SM-OPVs.[23,46,47] The small size of the fluorine atom generally renders it suitable for altering the energetics of molecular orbitals without introducing extraordinary steric

demands.[48–52] We examined how varying the fluorine group on an A unit influenced the properties of the solid-state ordering of the molecules and the charge carrier mobilities and photovoltaic performances in two different types of solar cells. The DTS(BTTh$_2$)$_2$-based compounds were first introduced as donor materials into the SM-OPVs, and subsequently, PSCs were prepared using the high mobility DTS(BTTh$_2$)$_2$ derivatives as a HTM without additives such as hygroscopic lithium bis(trifluoromethane sulfonyl) imide (Li-TFSi) and corrosive 4-tert-butylpyridine (t-BP). The properties of these solar cell devices were examined.

2. Results and discussion

2.1. Synthesis and physical properties

Scheme 1 illustrates the synthetic route to the five DTS (BTTh$_2$)$_2$ derivatives. Compounds 3 and 6 were reacted with a DTS ditin-compound in a Stille coupling condensation to provide the target molecules 0F and 4F, respectively. Compound 4 was prepared from the C–C coupling reaction of 4,7-dibromo-5-fluorobenzo[c][1,2,5]thiadiazole with (5'-hexyl-[2,2'-bithiophene]-5-yl)trimethylstannane. Compound 4 was coupled with a DTS mono-stannyl compound to afford compounds 9, which were then brominated using N-bromosuccinimide (NBS) and stannylated using hexamethylditin. Finally, 1F or 3F were prepared by C–C coupling reactions of compound 11 with 3 or 6, respectively. Compared with 2F, 0F and 1F showed better solubilities in chlorinated solvents, such as chloroform and chlorobenzene; however, 3F and 4F were poorly soluble in these solvents. The solubility of the compounds was related to the number of fluorine atom substitutions and the molecular symmetry generated by the presence of fluorine. A detailed description of the synthetic procedures and data are presented in the ESI.† All compounds were characterized by ^{1}H/^{13}C NMR spectroscopy, mass spectrometry, FT-IR spectrum, and elemental analysis (see the ESI†). The thermal properties of the compounds were evaluated using thermal gravimetric analysis (TGA) under a N$_2$ atmosphere. The 5% weight loss (T_d) of compounds occurred between 427 °C and 445 °C (Fig. S1, ESI†), indicating that these compounds provided excellent thermal stability.

2.2. Photophysical and electrochemical properties

The photophysical and electrochemical data are summarized in Table 1. Cyclic voltammetry (CV) was performed to study the electrochemical properties of 0–4F in a dichloromethane solution (Fig. 1(a)). The highest occupied molecular orbital (HOMO) and lowest unoccupied molecular orbital (LUMO) energy levels were estimated from the onset oxidation and reduction potential. As the fluorine substitution number increased, the HOMO and LUMO energy levels gradually decreased. The HOMO levels of 0F, 1F, 2F, 3F, and 4F were −5.06, −5.06, −5.12, −5.15, and −5.18 eV, respectively. All molecules showed good oxidative stability under two reversible redox couples in solution, suggesting their potential utility as electron-donating and hole-transporting materials. The energy bandgap (E_g^{elec}) obtained
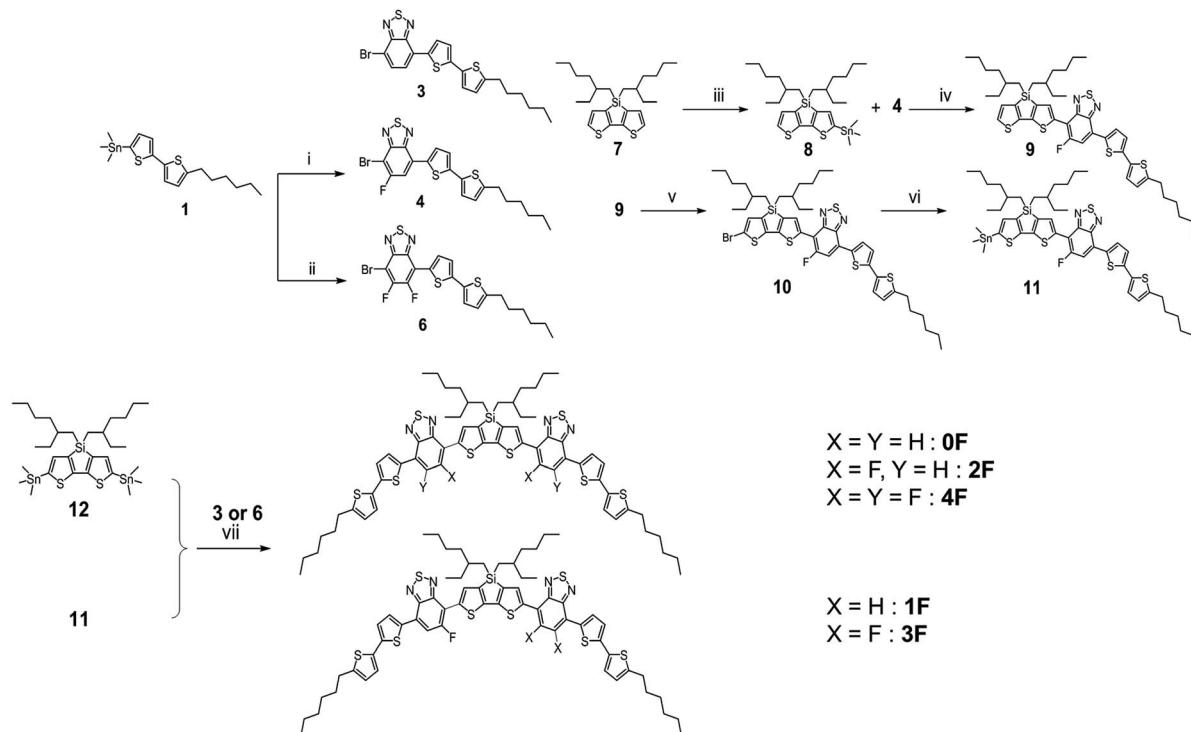
Scheme 1 Synthetic procedure used to prepare **0F**, **1F**, **2F**, **3F**, and **4F**: (i) Pd[PPh$_3$]$_4$, 4,7-dibromo-5-fluorobenzo[c][1,2,5]thiadiazole (2), toluene, 80 °C, 40 h. (ii) Pd[PPh$_3$]$_4$, 4,7-dibromo-5,6-difluorobenzo[c][1,2,5]thiadiazole (5), toluene, 160 °C, 1 h, microwave. (iii) n-BuLi, Me$_3$SnCl, THF, R.T., 12 h. (iv) Pd[PPh$_3$]$_4$, toluene, 160 °C, 1 h, microwave. (v) NBS, CHCl$_3$, R.T., 24 h. (vi) Pd[PPh$_3$]$_4$, hexamethylditin, toluene, 160 °C, 1 h, microwave. (vii) Pd[PPh$_3$]$_4$, toluene, 160 °C, 1 h, microwave.

from the HOMO and LUMO energy levels increased from **0F** (1.79 eV) to **4F** (1.85 eV).

The absorption spectra of **0–4F** in dilute chloroform solutions and in thin films are displayed in Fig. 1(b). The solution spectra revealed that increasing the number of fluorine substitutions resulted in a blue shift in both the absorption maximum (λ_{max}^{abs}) and onset points (λ_{onset}^{abs}); therefore, the onset absorption was blue-shifted by 27 nm from **0F** ($\lambda_{onset}^{abs} = 671$ nm) to **4F** ($\lambda_{onset}^{abs} = 644$ nm). In the solid state, each compound exhibited a broad optical absorption band with distinct high- and low-energy bands attributed to localized π–π^* transitions, and internal charge transfer respectively. The transition from the solution to the solid state in the thin films led to a red shift

in the optical absorption spectra and the emergence of a fine structure within the low-energy band. In particular, **1F–4F** displayed absorption bands that were more red-shifted than that of **0F**. This red shift was attributed to the planarization of the conjugated backbone and the formation of efficient intermolecular interactions within the film.[53–55] It should be noted that among the fluorinated molecules, the **2F** and **4F** films exhibited a greater extent of peak broadening and a bathochromic shift than did the **1F** and **3F** films. We surmised that the **2F** and **4F** films were characterized by a higher degree of ordered structures in the solid state. The distinctive molecular ordering in the films was reflected by the optical energy bandgaps (E_g^{opt}) of the compound. The E_g^{opt} values, estimated from the onset of the

Table 1 Optical and electrochemical measurements obtained from 0−4F

	Solution		Film							
	λ_{onset}^{abs} (nm)	λ_{max}^{abs} (nm)	λ_{onset}^{abs} (nm)	λ_{max}^{abs} (nm)	$\alpha(\lambda_{max})$ $\times 10^4$ cm^{-1}	E_g^{opt} (eV)	$\Delta\lambda_{onset}$[a] (nm)	LUMO (eV)	HOMO (eV)	E_g^{elec} (eV)
0F	671	591	730	670	6.41	1.70	59	−3.27	−5.06	1.79
1F	667	589	739	685	5.79	1.68	72	−3.30	−5.06	1.76
2F	663	587	759	683	5.64	1.63	96	−3.32	−5.12	1.80
3F	654	582	731	674	7.74	1.70	77	−3.32	−5.15	1.83
4F	644	579	745	663	5.15	1.66	101	−3.33	−5.18	1.85

[a] Obtained from the λ_{onset}^{abs} difference between the solution and film states.
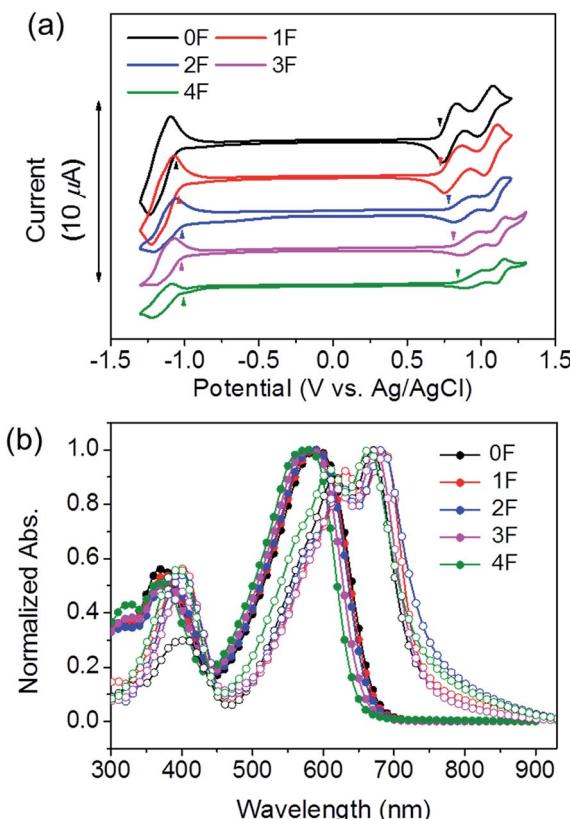
Fig. 1 (a) Cyclic voltammograms of **0–4F** dichloromethane solutions containing 0.1 mol L^{-1} Bu$_4$NPF$_6$ and a scan rate of 50 mV s^{-1}. (b) UV-vis absorption spectra of **0–4F** chloroform solutions (filled circles) and films (open circles).

film absorption, were 1.70, 1.68, 1.63, 1.70, and 1.66 eV for **0F**, **1F**, **2F**, **3F**, and **4F**. The compounds prepared with symmetric arrangements of an even number of fluorine atoms displayed lower E_g^{opt} values than the compounds prepared with an asymmetrical arrangement of odd numbers of fluorine atoms. These results differed from the CV results, probably because the CV measurements performed in solution did not reflect intermolecular interactions in the solid state. As shown in Table 1, **3F** had a higher absorption coefficient at the maximum absorption peak (7.74 × 10^4 cm^{-1}) as compared with other compounds, and **4F** showed the lowest value of 5.15 × 10^4 cm^{-1}. Given the high photon flux of the solar spectrum within the range 500–800 nm, such different absorption coefficients are expected to affect the short-circuit currents in solar cell devices.

2.3. Theoretical calculations

Density functional theory (DFT) calculations using Gaussian 09 at the B3LYP level with a 6-311(d,p) basis set were used to investigate the conformational and electronic properties of the compounds **0–4F**. The optimized structures and HOMO and LUMO orbital diagrams of all compounds are shown in Fig. 2 and S2.† The lowest energy conformational isomer was nearly coplanar and adopted a bent banana-type structure. **0–4F** commonly exhibited fully delocalized HOMOs and LUMOs
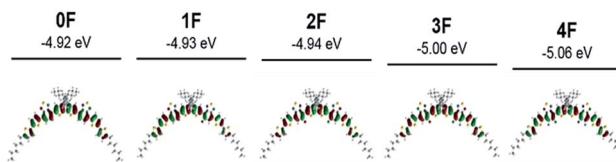
Fig. 2 Optimized banana type structures and their HOMO orbital diagrams for compounds **0F–4F** calculated by density functional theory (DFT).

across the molecular backbone. The calculated HOMO and LUMO values are summarized in Fig. S2.† As the number of fluorine atom substitutions increased, the HOMO and LUMO energy levels decreased, in agreement with the CV experimental results. **0F–2F** showed similar energy bandgaps of ~1.93 eV, and the energy bandgap increased slightly from **2F** (1.93 eV) to **4F** (1.98 eV). This trend differed from the results obtained from the absorption measurements, in which **2F** and **4F** exhibited lower E_g^{opt} values than the other compounds **0F**, **1F**, and **3F**. This disagreement most likely arose because the calculations assumed isolated molecules in the gas phase, whereas the optical properties were affected by intermolecular interactions in the solid state.[56–59] **2F** is known to assume an inverted banana shape in the crystal structure rather than a banana shape. The inverse banana favors effective π–π interactions.[60]

2.4. Charge transport

The charge transport characteristics of compounds **0–4F** were explored by fabricating and analyzing bottom gate/top contact field effect transistors. Considering the given HOMO levels of all compounds, Au source/drain electrodes were selected to render near-ohmic junctions for hole injection/extraction. The transfer characteristics of the compounds presented in Fig. 3 suggested the operation of a typical p-type dominant charge transport mechanism. The charge carrier mobility values of all compounds measured in the saturation mode are summarized in Fig. 3, together with the other transistor parameters. **2F** and **4F**, which featured symmetric fluorine substitutions, displayed obviously higher charge carrier mobilities compared to the other derivatives, with maximum mobilities of 0.22 cm^2 V^{-1} s^{-1} and 0.06 cm^2 V^{-1} s^{-1}, respectively. These mobility values were also higher than those of other D–A-type small molecule semiconductors, such as DTS-(PTTh$_2$)$_2$,[61] suggesting that a more favorable crystalline structure was achieved in films of DTS-(BTTh$_2$)$_2$, especially by introducing symmetric and even-numbered fluorine substitutions. The subthreshold swing (S) of the FET was related to the trap density by

$$N_{trap} \approx \left[\frac{qS \log(e)}{kT} - 1 \right] \frac{C_i}{q},$$

where q is the electronic charge, k is Boltzmann's constant, and T is the temperature.[62] Based on this equation, we estimated the interface trap densities of **0F**, **1F**, **2F**, **3F**, and **4F**-based OFETs to be 8.90 × 10^{12}, 6.52 × 10^{12}, 1.60 × 10^{12}, 5.62 × 10^{12}, and 3.86 × 10^{12} cm^{-2}, respectively. The estimated trap
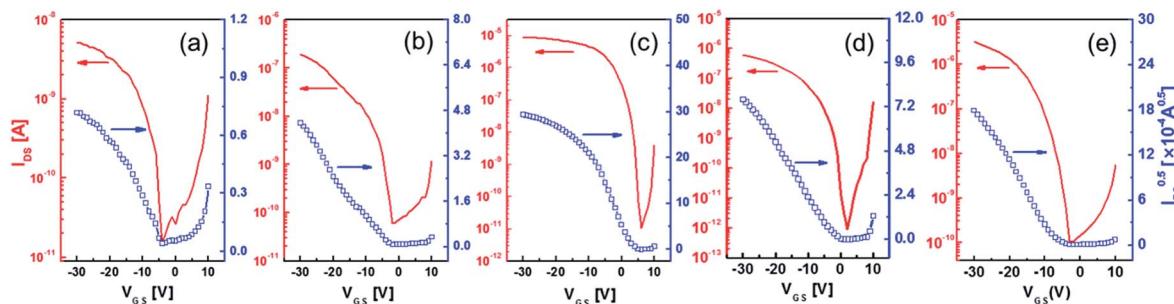
materials	μ [cm^2/(V·s)]		S [V/decade]	N_{trap} [×10^{12} cm^{-2}]	I_{on}/I_{off}
	Average	Maximum			
0F	3.68×10^{-5}	4.97×10^{-5}	2.87	8.90	~10^2
1F	1.23×10^{-3}	1.73×10^{-3}	2.12	6.52	~10^3
2F	0.176	0.217	0.56	1.60	~10^6
3F	3.17×10^{-3}	4.09×10^{-3}	1.83	5.62	~10^5
4F	5.34×10^{-2}	6.01×10^{-2}	1.28	3.86	~10^4

Fig. 3 Transfer characteristics of the OFETs prepared with (a) **0F**, (b) **1F**, (c) **2F**, (d) **3F**, and (e) **4F** films fabricated on OTS-modified substrates and the device performances of OFETs fabricated with **0F–4F**.

densities closely followed the trend in the charge carrier mobility, again confirming the presence of less energetic disorder in **2F** and **4F**.

Grazing incidence X-ray diffraction (GIXD) studies were conducted to understand the overall superiority of **2F** and **4F**, in terms of charge carrier mobility, compared to other derivatives.
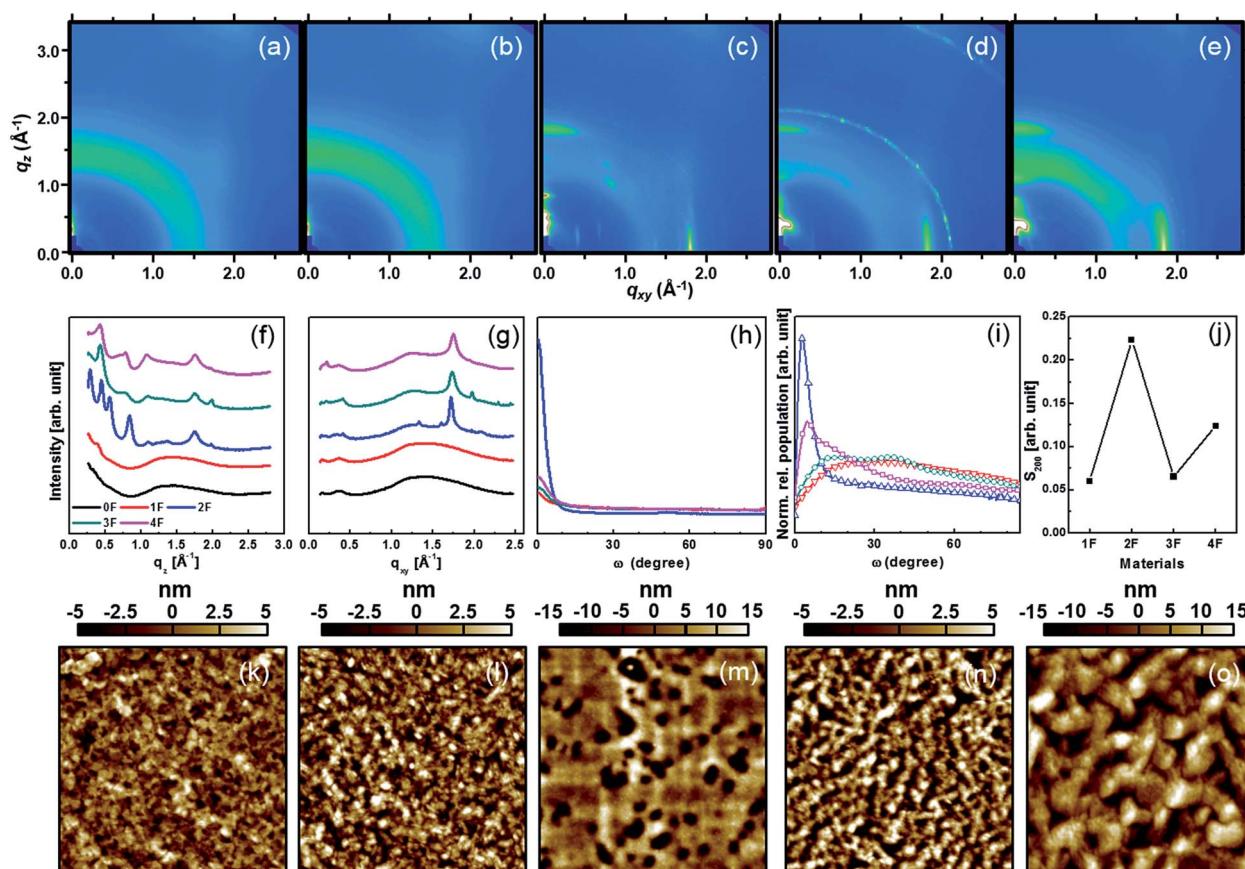
Fig. 4 2D-GIXD patterns of (a) **0F**, (b) **1F**, (c) **2F**, (d) **3F**, and (e) **4F** films, GIXD patterns in (f) out-of-plane and (g) in-plane directions, (h) the pole figures, (i) the pole figures multiplied by a factor of sin ω, and (j) the Herman's orientation factors as a function of the number of fluorine substitutions. AFM topography images of films consisting of (k) **0F**, (l) **1F**, (m) **2F**, (n) **3F**, and (o) **4F**.

Fig. 4 shows the 2D-GIXD patterns of all pristine compounds with their corresponding out-of-plane and in-plane profiles. The out-of-plane diffraction peaks contained a (001) diffraction peak, indicating that the DTS-(BTTh$_2$)$_2$ molecules stacked with their branched silyl alkyl groups on the substrate surface. The (001) peak intensity was highest for **2F** and **4F**. The 2D GIXD patterns obtained from **2F** and **4F** (as well as **3F**, in part) displayed numerous reflection spots along the q_z direction at a given q_{xy}, suggesting that the DTS-(BTTh$_2$)$_2$ molecules adopted a three-dimensional multi-layered structure.[63] Therefore, symmetric and even-numbered fluorine substitution patterns appeared to facilitate solid-state intermolecular interactions. A quantitative analysis of the crystal structures of all compounds was obtained by conducting pole figure analyses. Pole figures plot the distribution of diffraction peaks as a function of all possible crystallite orientations. The pole figures shown in Fig. 4(h) were normalized to the (200) scattering intensity of each sample in order to compare the orientations. The pole figures revealed that all the compound films adopted a preferential edge-on orientation, except for the case of **0F**, in which no diffraction peaks were observed. Most of the crystallites in the film were preferentially oriented within a polar angle of 10°, indicating the preferential formation of an edge-on orientation in all compounds. Geometrical effects in each sample were corrected by multiplying the intensity profile of the pole figure by a factor of sin ω, as shown in Fig. 4(i). Here, the relative population profile was normalized by the relative degree of crystallinity (rDoC) to facilitate a comparison among samples. The rDoC values of the compounds were calculated by integrating the relative population distributions, with consideration for the X-ray exposure time, beam footprint, sample thickness, and semiconductor volume fraction.[64] The calculated rDoC values were 1.0, 4.58, 1.46, and 3.1 for the **1F**, **2F**, **3F**, and **4F** films, respectively. The large rDoC values of **2F** and **4F** may have been induced by the significant enhancement in the intermolecular interactions. As shown in Fig. 4(i), the **2F** film exhibited a significant edge-on population, with a maximum at about ω = 6°. The **4F** film showed pretty well-developed edge-on population profiles, with a maximum at about ω = 15°, although a broad mixed population was present as well (ω > 20°). The other derivatives displayed very broad random distributions that corresponded to a nearly constant population across the range ω = 20–70°. In addition to the molecular orientation profiles, we calculated Herman's orientation factors (S_{200}) from the pole figures.[65] These values ranged from −0.5 to 1, where a high value indicated high-quality edge-on orientations among the crystallites. The S_{200} values of the compounds are summarized in Fig. 4(j), revealing that S_{200} reached its highest values for **2F** and **4F**. Morphological analyses of the AFM topographies were further conducted in parallel with the crystalline analyses. Fig. 4(k)–(o) shows the AFM height images of all compounds. **2F** and **4F** appeared to form very large continuous terrace-like crystalline features (>500 nm) whereas the other derivatives formed small nodular crystallites (100 nm) with a much less featured morphology. Overall, the crystalline/morphological analyses revealed that **2F** and **4F**, which featured symmetric/even-numbered fluorine substitution patterns, could adopt a very well-developed preferential edge-on orientation, thereby forming well-connected crystalline morphologies with percolation pathways for charge carriers that resulted in high charge carrier mobilities.

2.5. Solar cells

The solar cell properties were examined by fabricating bulk heterojunction solar cells with a device structure of ITO/PEIE/SM : PC$_{71}$BM/MoO$_3$/Ag. The photoactive layer was fabricated by spin-casting a solution of the compound : PC$_{71}$BM mixture dissolved in a chlorobenzene (CB) : 1,8-diiodooctane (DIO) (99.6 : 0.4 vol%) cosolvent. The optimized compound : PC$_{71}$BM ratio that gave the best solar cell performance was 3 : 2 for **0F**, **1F**, and **4F** and 6 : 5 for **3F** (see the ESI† for details about the device fabrication process). The photovoltaic performances of the prepared solar cell devices were investigated under simulated AM 1.5 G 1 Sun illumination (100 mW cm^{-2}). The current density–voltage (J–V) curves obtained from the solar cell devices are shown in Fig. 5(a), and the characteristic solar cell data are summarized in Table 2. **2F** provided the best solar cell performance, with the highest measured PCE value of 8.14%, a short circuit current (J_{sc}) of 15.37 mA cm^{-2}, a fill factor (FF) of 0.664, and an open-circuit voltage (V_{oc}) of 0.80 V. These values were 6 times the corresponding values obtained from the nonfluorinated compound **0F**. **0F** provided the lowest efficiency, 1.28%, with a J_{sc} of 4.21 mA cm^{-2}, a FF of 0.407, and a V_{oc} of 0.75 V. The single fluorine addition in going from **2F** to **3F** lowered the performance with respect to **2F**, affording a PCE of 6.84% for **3F**. **4F**, which had one more fluorine substitution than **3F**, exhibited a slightly higher efficiency of 7.06% compared to **3F**, mainly due to an increase in the V_{oc} (0.86 V) and FF (0.698) values. Therefore, the compounds that incorporated an even number of fluorine atoms, **2F** and **4F**, generally exhibited enhanced solar cell performances compared with the analogous compound bearing an odd number of fluorine atoms, **1F** and **3F**, primarily due to the improved V_{oc} and greater FF values. The higher V_{oc} values of the **2F** and **4F**-based solar cells agreed well with their deeper HOMO energy levels estimated from the electrochemical measurements (Table 1), and we concluded that symmetrical even-numbered fluorine substitutions increased V_{oc} more effectively. Overall, fluorinated compounds achieved improved FF values compared to the nonfluorinated **0F**. Among the fluorinated compounds, **2F** and **4F** showed higher FF values (**2F**: 0.664, **4F**: 0.698) compared with **1F** and **3F** (**1F**: 0.520, **3F**: 0.628). Fig. 5(b) shows the external quantum efficiency (EQE) spectra of the SMs-OPV devices. The EQE spectra of the devices reflected the absorption properties of each compound. **2F** exhibited larger EQE values than the other compounds. Its values were as high as 70% over the wavelength range 450–750 nm, which corresponded to the absorption spectrum of **2F**. These results were consistent with the observation that the **2F**-based device displayed the highest J_{sc} value among all solar cell devices. The $J_{sc,EQE}$ values obtained by integrating the EQE spectra were close to the J_{sc} values determined from the J–V curves (Table 2), indicating that the J–V measurements were highly reliable.
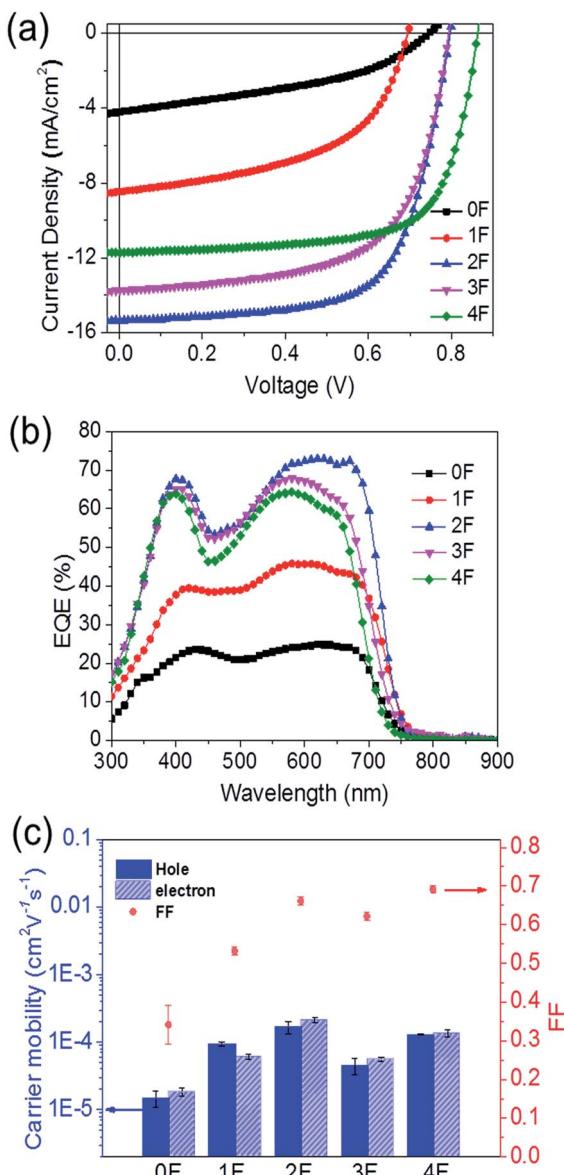
Fig. 5 (a) The current density–voltage (J–V) characteristics and (b) external quantum efficiency (EQE) curves based on the **0F−4F**/PC$_{71}$BM devices. (c) Comparisons of SCLC hole and electron mobilities of the **0F−4F**:PC$_{71}$BM films, and the fill factor values of **0F−4F**.

GIXD studies were conducted using the compound : PC$_{71}$BM blend films to understand the origin of the enhanced photovoltaic performances as a result of symmetric/even-numbered

fluorination. Fig. S3† presents the 2D-GIXD patterns obtained from all blend films with their corresponding out-of-plane and in-plane profiles as well as the results of the pole analyses. All blend films showed typical (l00) lamellar-type stacking and distinct (010) π–π stacking along the out-of-plane and in-plane directions, respectively, suggesting close-to-edge-on orientations among all compounds. The crystalline orientations of the compounds were analyzed qualitatively by comparing the relative population profiles normalized by the rDoC values of the pole figures, as summarized in Fig. S3(g).† Unlike the pristine compound samples discussed in the previous section, a (010) π–π stacking peak was obtained in the pole figure analysis because the **3F**-blend film did not give clear (l00) diffraction peaks. As shown in Fig. S3(g),† the **4F**-blend film exhibited a relatively large edge-on population with a pronounced increase in the population at ω > 60°. All other blend films showed distinct edge-on populations only for ω > 80°. These results suggested that overall, all compounds adopted nearly randomly-oriented crystalline structures, with a slightly larger fraction of the edge-on population. The large number of fluorine moieties in **4F** appeared to facilitate the formation of edge-on orientations among the compounds, even in the blend films. This effect will be further explored by our group in the near future. The values of rDoC are summarized in Fig. S3(h)† and display a clear decreasing trend in the order of **2F** > **4F** > **3F** > **1F**. The relatively large rDoC values of **2F** and **4F** suggested that the nanocrystalline domains of the compounds with symmetric/even-numbered fluorine substitutions were packed more densely in a defect-free manner, which could enhance percolated charge transport, as estimated from FF values. We argue that rather than merely indicating slightly different orientations among the compounds, the rDoC values have a dramatic effect on solar cell performances.

The influence of fluorination on the BHJ solar cell properties was investigated by collecting transmission electron microscopy (TEM) and atomic force microscopy (AFM) images of the compound : PC$_{71}$BM BHJ film nanostructures in the solar cell devices. Fig. S4† shows the TEM and AFM surface topographic images of the BHJ blend films. The **0F** and **1F** blend films revealed large-scale phase separation, hundred nanometer-scale PC$_{71}$BM-rich domains (Fig. S4(a) and (b),† darker phase), and a relatively high surface root-mean-square (RMS) roughness over the range 1.5–3.9 nm, as shown in Fig. S4(f) and (g).† By contrast, the **2–4F** blend films displayed well-defined ten nanometer-scale phase separation and interpenetrating

Table 2 The device performances of the BHJ SM solar cells

Active layer	V_{oc}^{a} [V]	J_{sc}^{a} [mA cm^{-2}]	J_{sc}^{b} [mA cm^{-2}]	FF^{a}	PCE^{a} [%]	PCE$_{max}$ [%]
0F	0.76 ± 0.02	4.55 ± 0.41	5.01	0.34 ± 0.05	1.16 ± 0.09	1.28
1F	0.70 ± 0.01	8.23 ± 0.24	9.30	0.53 ± 0.01	3.02 ± 0.03	3.07
2F	0.81 ± 0.01	14.96 ± 0.39	14.37	0.66 ± 0.01	7.98 ± 0.09	8.14
3F	0.78 ± 0.01	13.42 ± 0.22	12.84	0.62 ± 0.01	6.59 ± 0.14	6.84
4F	0.86 ± 0.02	11.56 ± 0.15	11.51	0.69 ± 0.01	6.86 ± 0.14	7.06

^{a} Average data with standard deviations obtained from nine devices. ^{b} The value extracted from the EQE spectra.

networks. The **2F** and **4F** films formed fine fibril structures, although their sizes and shapes differed, suggesting improved intermolecular packing and long-range ordered structures in the **2F** and **4F** blend films.

The charge carrier mobilities of the compound : PC$_{71}$BM blend films were measured using the space charge limited current (SCLC) method. The **2F** blend film exhibited the highest hole mobility of 1.70×10^{-4} cm^2 V^{-1} s^{-1}, followed by **4F** (1.30×10^{-4} cm^2 V^{-1} s^{-1}). **1F** and **3F** exhibited lower hole mobility values of 9.38×10^{-5} and 4.47×10^{-5} cm^2 V^{-1} s^{-1}, respectively. **0F** showed the lowest hole mobility of 1.50×10^{-5} cm^2 V^{-1} s^{-1}. These results agreed well with the OTFT mobility obtained from the pristine compound, suggesting that the intermolecular packing structure of the compound was retained in the BHJ film. The electron mobilities in the blend film followed a trend similar to the hole mobility trend. The electron mobility was highest in the **2F** blend film, with a value of 2.11×10^{-4} cm^2 V^{-1} s^{-1}, and **4F** revealed a slightly higher electron mobility of 1.35×10^{-4} cm^2 V^{-1} s^{-1} compared to **1F** and **3F**. **1F** and **3F** exhibited similar electron mobility values of 6.06×10^{-5} cm^2 V^{-1} s^{-1} and 5.60×10^{-5} cm^2 V^{-1} s^{-1}, respectively. **0F** also showed the lowest electron mobility of 1.39×10^{-5} cm^2 V^{-1} s^{-1}. The poor charge carrier transporting properties of **0F** were correlated with the amorphous packing structure in the film, as indicated in the GIXD results. All compounds displayed similar hole-to-electron mobility ratios within the range 1–1.5, indicating good charge balance between the holes and electrons in all solar cell devices. The different charge mobilities measured among the compounds could affect the FFs in the solar cells. Fig. 5(c) indicated a change in the SCLC hole and electron mobilities as a function of the fluorine substitution. Both mobilities were influenced by the symmetricity and numbers of the fluorine atom substitutions. Notable correlations between the FF values of the solar cells and the charge carrier mobilities were observed. Among the fluorinated compounds, **2F** and **4F** showed better transport properties and, thus, FFs compared with **1F** and **3F**. A comparison of the absorption coefficients of the compounds revealed that the J_{sc} values of the compounds depended on the charge mobility. The effects of the molecular arrangements and mobilities on the photocurrent properties of solar cells were estimated by comparing the J_{sc} values and the absorption properties of the compounds. Fig. S7† shows pristine film absorption profiles for **0F–4F** (determined by the absorption coefficient and the film thickness, thickness of each film was adjusted to 70 ± 3 nm). The ratios of J_{sc} to integrated absorption were found to decrease in the order of **2F** > **4F** > **3F** > **1F** > **0F**, in good agreement with the SCLC mobility trend observed across **0–4F**. We expected that the remarkably different solar cell performances among the molecules were correlated with the improved charge transport properties, which may be influenced by the fluorine substitutions on the accepting BT units. As a result, the overall solar cell efficiency depended significantly on the symmetry of the fluorine incorporation pattern, and number (even or odd) of fluorine atom substitutions. The compounds **2F** and **4F** achieved higher solar cell performances compared with **1F** and **3F**.

Differences in the nanoscale morphology and charge transport properties of **0–4F** pointed to the acceptor BT and its

fluorine substitution pattern, which played a critical role in the intermolecular interactions and packing structure of the thin film.

The solid state packing structure depends on the molecular structure, relative energy, and electrostatics of the conformations adopted by the compound **0–4F**. The equilibrium geometries and dipole moments of **0–4F** in the gas phase were calculated using DFT methods. Fig. 6 shows the optimized structures of the possible molecular conformations, tabulated energies, and dipole moments of **0–4F**. All compounds assumed a banana-shaped bent conformation as the energetically most stable structure. These results differed from the results obtained from the single crystal X-ray diffraction studies of **2F**, in which the conjugated backbone formed an inverted banana shape with a high planarity and packed in a slip-stack manner. The inverted banana shape conformation induced high intermolecular overlap among the conjugated backbones, which facilitated π–π overlapping.[58] Although a large fraction of **2F** is present in a banana shape in the gas state, the conformation switches to an inverted banana shape in the solid state, thereby favoring efficient intermolecular interactions. The other compounds, **0F**, **1F**, **3F**, and **4F**, may behave similarly and undergo similar packing processes in the film state, although their fluorine substitution patterns influenced the intermolecular interactions. We compared the energy differences among the different conformers. A large energy increase from the banana shape to another conformation would suggest that few of the compounds would make this transition, and the banana shape would dominate. As shown in Fig. 6, **0F** showed the highest energy increase from the banana shape to the inverted banana shape (6.53 kJ mol^{-1}), followed by **1F** (4.3 kJ mol^{-1}). Notably, as more fluorine atoms were incorporated from **0F** to **4F**, the compounds displayed a smaller energy difference between the banana and inverted banana shapes, indicating that a greater fraction of the fluorinated compounds was present in an inverted banana shape, which favored efficient π–π interactions in the thin film. The predicted film conformations agreed with the experimental GIXD results, which indicated that **0F** formed amorphous structures and provided the lowest charge carrier mobility in the OTFT studies. The energy difference between the banana shape and the zigzag conformation decreased from **0F** to **4F**. Therefore, the relative energy difference between the zigzag and the inverted banana shape was smaller for the fluorinated compounds. **4F** had the smallest value of 0.36 kJ mol^{-1}, whereas **0F** had the largest value of 3.39 kJ mol^{-1}. The energy differences of **1F** and **3F** depended on the molecular shape. The zigzag-shaped conformation formed by rotating the more fluorinated BT units was lower in energy than the conformation of the corresponding shape formed by rotating the non- or less fluorinated BT. Fig. 6 presents the magnitude and direction of the dipole moment. The compounds with a symmetrical conformation (**0F**, **2F**, and **4F**) showed a dipole direction perpendicular to the linear molecule, whereas the asymmetrically shaped compounds **1F** and **3F** exhibited distinct dipole directions that depended on the conformation. In the zigzag conformation, **1F** and **3F** assumed two distinct isomers due to their asymmetric chemical

	Banana	Zigzag	Inverted banana
0F			
ΔE / |dipole|	0 / 2.56 debye	3.14 kJ/mol / 1.43 debye	6.53 kJ/mol / 3.43 debye
1F			
ΔE / |dipole|	0 / 2.80 debye	3.45 kJ/mol / 0.97 debye / 1.15 kJ/mol / 2.39 debye	4.43 kJ/mol / 2.24 debye
2F			
ΔE / |dipole|	0 / 1.78 debye	1.16 kJ/mol / 0.71 debye	2.13 kJ/mol / 0.71 debye
3F			
ΔE / |dipole|	0 / 1.47 debye	1.12 kJ/mol / 2.05 debye / 0.51 kJ/mol / 2.01 debye	1.46 kJ/mol / 2.07 debye
4F			
ΔE / |dipole|	0 / 1.05 debye	0.44 kJ/mol / 0.40 debye	0.80 kJ/mol / 0.44 debye
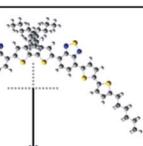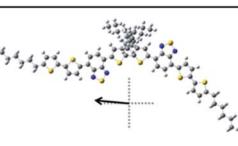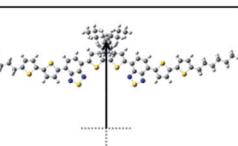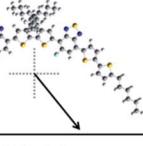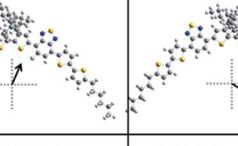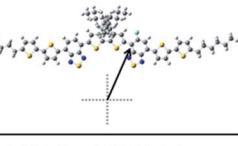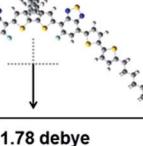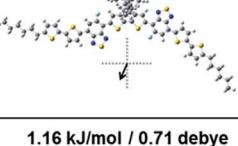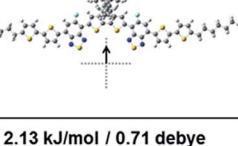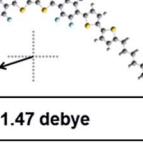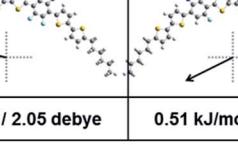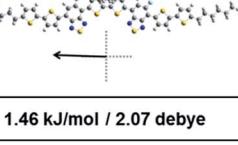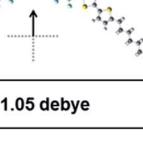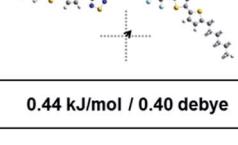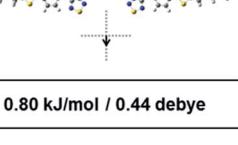
Fig. 6 Optimized molecular conformations, energy difference from the banana shape conformer of each compound and their dipole moments for compounds 0F–4F.

structures, and the isomers displayed different dipole moments relative to one another. The asymmetric **1F** and **3F** molecules displayed more diverse dipole moments and directions, as well as a greater number of conformations, which could be related to their poor crystalline properties in the thin film state, as shown in the GIXD patterns (Fig. 4). The **1F** and **3F** diffraction patterns did not reveal any notable peaks corresponding to the long-range ordering, such as the lamellar-like packing structures. By contrast, peaks due to the alkyl stacking interactions as well as the well-defined π–π stacking interactions were observed in the **2F** and **4F** films. The molecules tended to organize themselves in such a way as to minimize the net dipole moment. Molecules with a symmetric linear conformation favorably assembled in an antiparallel manner and efficiently formed a lamellar-like packing structure. Although all compounds with the inverted banana conformation could efficiently dimerize and form a lamellar-like structure, molecules with different conformations were expected to coexist in a certain distribution. Because the zigzag shapes were relatively stable compared with the inverted banana shape, they were present in some fraction in

the thin film. The zigzag shape was able to form more favorable π–π stacking structures compared with the banana shape because it was somewhat linear. The zigzag structures in **1F** and **3F** may not form an effective alkyl stacking due to their diverse dipole moments and orientations present in these molecular distributions. For example, a combination of inverted banana and zigzag configurations (**1F** zigzag-2) in **1F** can form a lamellar-like packing structure that aligns the dipole moments of the molecules in a single direction, thereby increasing the energy of the system. The broad distribution of conformers and the relatively large dipole moments of **1F** and **3F** increase the probability of assuming this type of molecular structure, consistent with the observed low crystallinities of **1F** and **3F** in the thin film state. By contrast, **2F** and **4F** were present in a narrow distribution of conformations, and the dipole moments were lower than those of **1F** and **3F**. Therefore, the probability of forming alkyl stacking interactions among the different conformations in **2F** (or **4F**) was relatively low. Even dimerization between the different conformations yielded an overall dipole and energy enhancements that were not as high

as the corresponding values for **1F** and **3F**. The narrower distribution of conformers in **2F** and **4F** and their more favorable dipole–dipole interactions suggested that these compounds should display better assembly properties in the thin film states.

The advantages of the **2F** molecular conformations, packing structures, and mobility were exploited by preparing planar heterojunction perovskite solar cells (PHJ PSCs) using **2F** as a dopant-free hole transporting material (HTM). The fabricated cell has the architecture of $FTO/TiO_2/MAPbI_3/HTM/Au$. The device preparation steps are described in detail in the ESI.† For comparison purposes, a PSC was fabricated by replacing 2F with **0F** in the same device structure prepared under otherwise identical processing conditions. Fig. 7(a) shows a representative SEM cross-sectional image of the **2F**-based PHJ PSC. Fig. 7(b) displays the corresponding energy band diagrams of each component, revealing that the holes generated in $MAPbI_3$ could be effectively transported to the **0F** and **2F** HTMs. The photovoltaic performances of these two solar cell devices under a simulated AM 1.5 G 1 Sun illumination (100 mW cm^{-2}) are represented by the current density–voltage (J–V) curves plotted

in Fig. 7(c) and (d). The photovoltaic properties of the solar cells are summarized in Table 3. The PHJ PSC prepared with **2F** provided a PCE (η) of 14.2% under forward scan conditions (scan rate = 50 mV s^{-1}), with an open circuit voltage (V_{oc}) of 0.99 V, a short circuit current density (J_{sc}) of 20.0 mA cm^{-2}, and a fill factor (FF) of 0.72. An efficiency of 14.7% was obtained under reverse scan conditions, with a V_{oc} of 0.99 V, a J_{sc} of 20.1 mA cm^{-2}, and a FF of 0.74, thereby yielding an average PCE (η_{avg}) of 14.45%. By contrast, the parameters obtained from the **0F**-based device were all notably lower. The PSC was characterized by a V_{oc} of 0.93 V, a J_{sc} of 17.0 mA cm^{-2}, and a FF of 0.54,

Table 3 The device performances of the perovskite solar cells

|	Scan direction	V_{oc} [V]	J_{sc} [mA cm^{-2}]	FF	PCE [%]	PCE (η_{avg})
0F	Forward	0.93	17.0	0.54	8.50	8.95
	Reverse	0.94	17.4	0.57	9.40	
2F	Forward	0.99	20.0	0.72	14.20	14.45
	Reverse	0.99	20.1	0.74	14.70	
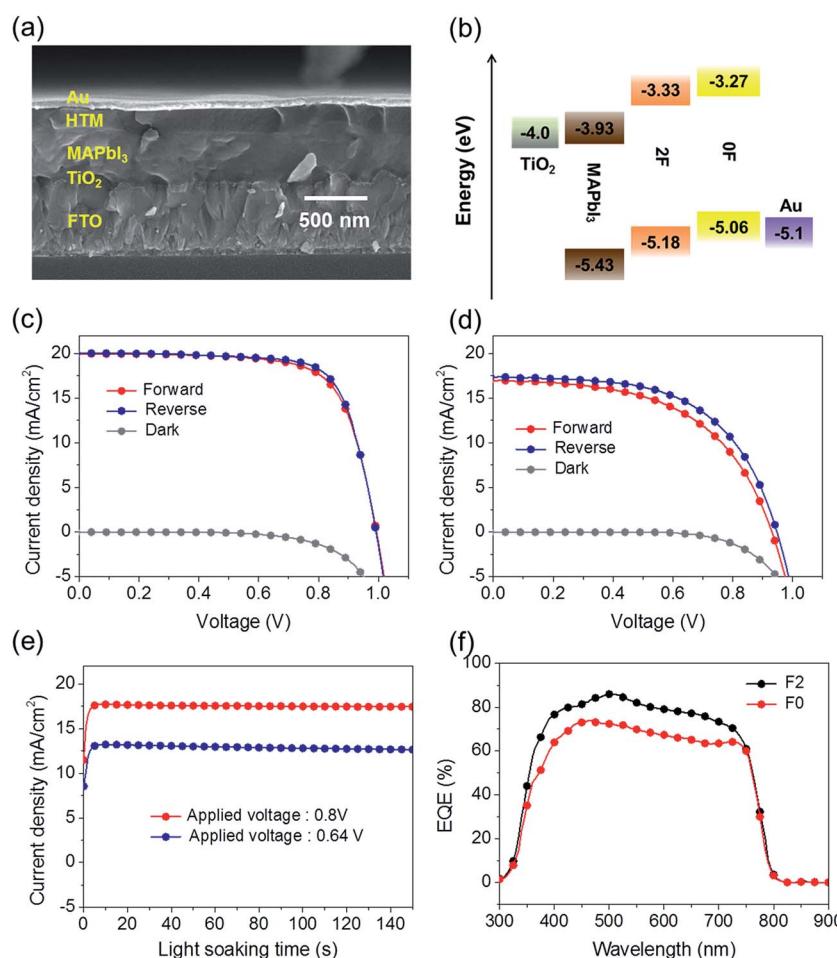
Fig. 7 (a) The SEM cross-section image and (b) energy diagram of the perovskite solar cell device. The current density–voltage (J–V) characteristics based on the solar cells with (c) **2F** and (d) **0F**. (e) current density (J) variation of the **0F** and **2F** based PSCs with a light soaking (1 Sun) time under the applied bias voltage (V_{opt}) at maximum power point (P_{max}) and (f) EQE spectra of the **0F** and **2F** based PSCs.

yielding an efficiency of 8.5% under the forward scan conditions and a V_{oc} of 0.94 V, a J_{sc} of 17.4 mA cm^{-2}, a FF of 0.57, and an efficiency of 9.4% under reverse scan conditions; the resulting η_{avg} was 8.95%. It is notable that the **2F** based PSC device shows much smaller J–V hysteresis compared with the PSC with **0F**. Fig. 7(e) shows the current density variation of **0F** and F2 based devices with a light soaking time under optimal bias voltage (V_{opt}) (V_{opt} = 0.64 V for the **0F** based device and V_{opt} = 0.80 V for the **2F** based device) of maximum power (P_{max}) point under 1 Sun (100 mW cm^{-2}) illumination of continuous light. Both devices exhibit the same tendency that the current density (J) is quickly saturated with a light soaking time and maintains stability under the current experimental time window. Fig. S5† shows histograms of the efficiencies and the PCEs averaged from 40 devices are 5.14 ± 2.08% and 11.18 ± 1.89% for the **0F** and **2F** PSCs, respectively. The superior performance of the **2F**-based device was attributed to the enhancement in the FF value (averaged from forward and reverse scans) from 55.6% to 72.6% and the J_{sc} value from 17 to 20 mA cm^{-2}. The higher V_{oc} of the **2F**-based device, which was 50 mV higher than the value measured from **0F**, is attributed to the lower HOMO energy level of **2F** compared with **0F**.

The improved photocurrent properties in the **2F** device most likely arose from the higher hole transporting ability of **2F**. The EQE spectra shown in Fig. 7(f) revealed that the PHJ PSC prepared with **2F** offered a better EQE value in the range of 350–800 nm compared with the **0F** device. The J_{sc} of the **2F** device was calculated by integrating the EQE data across the AM1.5G solar spectrum (100 mW cm^{-2}) and was found to be 19.3 mA cm^{-2} higher than the value of 16.6 mA cm^{-2} obtained from the **0F**-based device, a difference that was comparable to the difference in J_{sc} obtained from the respective J–V curves.

3. Conclusions

Four DTS(BTTh$_2$)$_2$ small molecules with different fluorine substitution patterns were prepared, and their charge transport and solar cell properties were examined. The optical, electronic, and morphological properties of these compounds were compared to understand the significance and effect of the symmetricity and number of fluorine atoms incorporated. **2F** and **4F** displayed better edge-on orientations and higher crystalline properties in the film state compared with **1F** and **3F**; thus, **2F** achieved the highest OTFT mobility of 0.217 cm^2 V^{-1} s^{-1} among the compounds. When blended with PC$_{71}$BM, **0F–4F** exhibited similar random orientations; however, **2F** and **4F**, which featured symmetric and even-numbered fluorine substitution patterns, displayed greater order among the nanocrystalline domains than **1F** or **3F**, resulting in higher charge transport properties in the blend films. As a result, **2F** achieved the highest photovoltaic performances with an 8.14% efficiency due to its improved FF and photocurrent properties. Furthermore, the PSC fabricated using **2F** as a dopant-free HTM displayed a high PCE of 14.45% by virtue of its high charge transport properties, which were significantly better than those obtained from the corresponding **0F**-based PSC device (8.95%). The low variation in the local dipole moment and the narrow

distribution of **2F** conformers facilitated intermolecular interactions, which could enhance/drive crystal formation in the solid state compared with **1F** and **3F**. The results suggested that the molecular conformations favored upon introducing substitution groups, such as fluorine, are important factors in the design of high-performance small-molecule materials: in addition to the electron-donating or -accepting properties of a molecular building blocks, factors that affect the intermolecular interactions in the solid state must be considered during the design of push–pull-type charge transporting materials.

References

1 K. H. Cheon, J. Cho, Y. H. Kim and D. S. Chung, *ACS Appl. Mater. Interfaces*, 2015, **7**, 14004–14010.

2 V. Grenier, A. S. Walker and E. W. Miller, *J. Am. Chem. Soc.*, 2015, **137**, 10894–10897.

3 M. Gross, D. C. Muller, H.-G. Nothofer, U. Scherf, D. Neher, C. Brauchle and K. Meerholz, *Nature*, 2000, **405**, 661–665.

4 V. G. Kozlov, V. Bulovic, P. E. Burrows and S. R. Forrest, *Nature*, 1997, **389**, 362–364.

5 J. R. Lawrence, G. A. Turnbull and I. D. W. Samuel, *Appl. Phys. Lett.*, 2002, **80**, 3036.

6 G. Li, V. Shrotriya, J. Huang, Y. Yao, T. Moriarty, K. Emery and Y. Yang, *Nat. Mater.*, 2005, **4**, 864–868.

7 G. Long, X. Wan, B. Kan, Y. Liu, G. He, Z. Li, Y. Zhang, Y. Zhang, Q. Zhang, M. Zhang and Y. Chen, *Adv. Energy Mater.*, 2013, **3**, 639–646.

8 J. Yao, C. Yu, Z. Liu, H. Luo, Y. Yang, G. Zhang and D. Zhang, *J. Am. Chem. Soc.*, 2016, **138**, 173–185.

9 X. Zhang, H. Bronstein, A. J. Kronemeijer, J. Smith, Y. Kim, R. J. Kline, L. J. Richter, T. D. Anthopoulos, H. Sirringhaus, K. Song, M. Heeney, W. Zhang, I. McCulloch and D. M. DeLongchamp, *Nat. Commun.*, 2013, **4**, 2238.

10 Y. Liu, Z. A. Page, T. P. Russell and T. Emrick, *Angew. Chem., Int. Ed.*, 2015, **54**, 11485–11489.

11 J. Mei, H. Kim do, A. L. Ayzner, M. F. Toney and Z. Bao, *J. Am. Chem. Soc.*, 2011, **133**, 20130–20133.

12 J. W. Sun, J. Y. Baek, K.-H. Kim, C.-K. Moon, J.-H. Lee, S.-K. Kwon, Y.-H. Kim and J.-J. Kim, *Chem. Mater.*, 2015, **27**, 6675–6681.

13 A. T. Yiu, P. M. Beaujuge, O. P. Lee, C. H. Woo, M. F. Toney and J. M. Frechet, *J. Am. Chem. Soc.*, 2012, **134**, 2180–2185.

14 Y. Diao, B. C. Tee, G. Giri, J. Xu, H. Kim do, H. A. Becerril, R. M. Stoltenberg, T. H. Lee, G. Xue, S. C. Mannsfeld and Z. Bao, *Nat. Mater.*, 2013, **12**, 665–671.

15 S. Hong, H. Kang, G. Kim, S. Lee, S. Kim, J.-H. Lee, J. Lee, M. Yi, J. Kim, H. Back, J.-R. Kim and K. Lee, *Nat. Commun.*, 2016, **7**, 10279.

16 J. Huang, C.-Z. Li, C.-C. Chueh, S.-Q. Liu, J.-S. Yu and A. K. Y. Jen, *Adv. Energy Mater.*, 2015, **5**, 1500406.

17 S. Mandal, G. Dell'Erba, A. Luzio, S. G. Bucella, A. Perinot, A. Calloni, G. Berti, G. Bussetti, L. Duò, A. Facchetti, Y.-Y. Noh and M. Caironi, *Org. Electron.*, 2015, **20**, 132–141.

18 T. Sekitani, U. Zschieschang, H. Klauk and T. Someya, *Nat. Mater.*, 2010, **9**, 1015–1022.

19 H. Youn, T. Lee and L. J. Guo, *Energy Environ. Sci.*, 2014, **7**, 2764–2770.

20 Y. Lin, Y. Li and X. Zhan, *Chem. Soc. Rev.*, 2012, **41**, 4245–4272.

21 B. Kan, M. Li, Q. Zhang, F. Liu, X. Wan, Y. Wang, W. Ni, G. Long, X. Yang, H. Feng, Y. Zuo, M. Zhang, F. Huang, Y. Cao, T. P. Russell and Y. Chen, *J. Am. Chem. Soc.*, 2015, **137**, 3886–3893.

22 B. Kan, Q. Zhang, M. Li, X. Wan, W. Ni, G. Long, Y. Wang, X. Yang, H. Feng and Y. Chen, *J. Am. Chem. Soc.*, 2014, **136**, 15529–15532.

23 A. K. K. Kyaw, D. H. Wang, V. Gupta, W. L. Leong, L. Ke, G. C. Bazan and A. J. Heeger, *ACS Nano*, 2013, **7**, 4569–4577.

24 K. H. Jung, S. Y. Bae, K. H. Kim, M. J. Cho, K. Lee, Z. H. Kim, D. H. Choi, D. H. Lee, D. S. Chung and C. E. Park, *Chem. Commun.*, 2009, 5290–5292.

25 J. I. Park, J. W. Chung, J. Y. Kim, J. Lee, J. Y. Jung, B. Koo, B. L. Lee, S. W. Lee, Y. W. Jin and S. Y. Lee, *J. Am. Chem. Soc.*, 2015, **137**, 12175–12178.

26 T. Yamamoto and K. Takimiya, *J. Am. Chem. Soc.*, 2007, **129**, 2224–2225.

27 M. J. Kang, I. Doi, H. Mori, E. Miyazaki, K. Takimiya, M. Ikeda and H. Kuwabara, *Adv. Mater.*, 2011, **23**, 1222–1225.

28 H. Minemawari, T. Yamada, H. Matsui, J. Tsutsumi, S. Haas, R. Chiba, R. Kumai and T. Hasegawa, *Nature*, 2011, **475**, 364–367.

29 Y. Yuan, G. Giri, A. L. Ayzner, A. P. Zoombelt, S. C. Mannsfeld, J. Chen, D. Nordlund, M. F. Toney, J. Huang and Z. Bao, *Nat. Commun.*, 2014, **5**, 3005.

30 T. Umeyama and H. Imahori, *J. Mater. Chem. A*, 2014, **2**, 11545–11560.

31 Z.-G. Zhang and J. Wang, *J. Mater. Chem.*, 2012, **22**, 4178.

32 A. Ajayaghosh, *Chem. Soc. Rev.*, 2003, **32**, 181–191.

33 B. Albinsson, M. P. Eng, K. Pettersson and M. U. Winters, *Phys. Chem. Chem. Phys.*, 2007, **9**, 5847–5864.

34 H. Zhou, L. Yang and W. You, *Macromolecules*, 2012, **45**, 607–632.

35 Y. Hua, B. Xu, P. Liu, H. Chen, H. Tian, M. Cheng, L. Kloo and L. Sun, *Chem. Sci.*, 2016, **7**, 2633–2638.

36 Y. Liu, Z. Hong, Q. Chen, H. Chen, W. H. Chang, Y. M. Yang, T. B. Song and Y. Yang, *Adv. Mater.*, 2016, **28**, 440–446.

37 P. Qin, H. Kast, M. K. Nazeeruddin, S. M. Zakeeruddin, A. Mishra, P. Bäuerle and M. Grätzel, *Energy Environ. Sci.*, 2014, **7**, 2981–2985.

38 C. Steck, M. Franckevičius, S. M. Zakeeruddin, A. Mishra, P. Bäuerle and M. Grätzel, *J. Mater. Chem. A*, 2015, **3**, 17738–17746.

39 N. Cho, K. Song, J. K. Lee and J. Ko, *Chem.–Eur. J.*, 2012, **18**, 11433–11439.

40 K. Sun, Z. Xiao, S. Lu, W. Zajaczkowski, W. Pisula, E. Hanssen, J. M. White, R. M. Williamson, J. Subbiah, J. Ouyang, A. B. Holmes, W. W. Wong and D. J. Jones, *Nat. Commun.*, 2015, **6**, 6013.

41 T. S. van der Poll, J. A. Love, T. Q. Nguyen and G. C. Bazan, *Adv. Mater.*, 2012, **24**, 3646–3649.

42 Q. Zhang, B. Kan, F. Liu, G. Long, X. Wan, X. Chen, Y. Zuo, W. Ni, H. Zhang, M. Li, Z. Hu, F. Huang, Y. Cao, Z. Liang, M. Zhang, T. P. Russell and Y. Chen, *Nat. Photonics*, 2015, **9**, 35–41.

43 J. J. Intemann, K. Yao, F. Ding, Y. Xu, X. Xin, X. Li and A. K. Y. Jen, *Adv. Funct. Mater.*, 2015, **25**, 4889–4897.

44 A. Ojala, A. Petersen, A. Fuchs, R. Lovrincic, C. Pölking, J. Trollmann, J. Hwang, C. Lennartz, H. Reichelt, H. W. Höffken, A. Pucci, P. Erk, T. Kirchartz and F. Würthner, *Adv. Funct. Mater.*, 2012, **22**, 86–96.

45 C. Sutton, C. Risko and J.-L. Brédas, *Chem. Mater.*, 2016, **28**, 3–16.

46 V. Gupta, A. K. Kyaw, D. H. Wang, S. Chand, G. C. Bazan and A. J. Heeger, *Sci. Rep.*, 2013, **3**, 1965.

47 Y. Sun, J. Seifter, L. Huo, Y. Yang, B. B. Y. Hsu, H. Zhou, X. Sun, S. Xiao, L. Jiang and A. J. Heeger, *Adv. Energy Mater.*, 2015, **5**, 1400987.

48 X. Liu, Y. Sun, B. B. Hsu, A. Lorbach, L. Qi, A. J. Heeger and G. C. Bazan, *J. Am. Chem. Soc.*, 2014, **136**, 5697–5708.

49 T. L. Nguyen, H. Choi, S. J. Ko, M. A. Uddin, B. Walker, S. Yum, J. E. Jeong, M. H. Yun, T. J. Shin, S. Hwang, J. Y. Kim and H. Y. Woo, *Energy Environ. Sci.*, 2014, **7**, 3040–3051.

50 A. C. Stuart, J. R. Tumbleston, H. Zhou, W. Li, S. Liu, H. Ade and W. You, *J. Am. Chem. Soc.*, 2013, **135**, 1806–1815.

51 M. Zhang, X. Guo, S. Zhang and J. Hou, *Adv. Mater.*, 2014, **26**, 1118–1123.

52 H. Zhou, L. Yang, A. C. Stuart, S. C. Price, S. Liu and W. You, *Angew. Chem., Int. Ed.*, 2011, **50**, 2995–2998.

53 J. S. Kim, Z. Fei, S. Wood, D. T. James, M. Sim, K. Cho, M. J. Heeney and J.-S. Kim, *Adv. Energy Mater.*, 2014, **4**, 1400527.

54 P. M. Oberhumer, Y.-S. Huang, S. Massip, D. T. James, G. Tu, S. Albert-Seifried, D. Beljonne, J. Cornil, J.-S. Kim, W. T. S. Huck, N. C. Greenham, J. M. Hodgkiss and R. H. Friend, *J. Chem. Phys.*, 2011, **134**, 114901.

55 R. Steyrleuthner, M. Schubert, I. Howard, B. Klaumünzer, K. Schilling, Z. Chen, P. Saalfrank, F. Laquai, A. Facchetti and D. Neher, *J. Am. Chem. Soc.*, 2012, **134**, 18303–18317.

56 J. Clark, J.-F. Chang, F. C. Spano, R. H. Friend and C. Silva, *Appl. Phys. Lett.*, 2009, **94**, 163306.

57 A. T. Haedler, H. Misslitz, C. Buehlmeyer, R. Q. Albuquerque, A. Kohler and H. W. Schmidt, *ChemPhysChem*, 2013, **14**, 1818–1829.

58 R. Noriega, J. Rivnay, K. Vandewal, F. P. V. Koch, N. Stingelin, P. Smith, M. F. Toney and A. Salleo, *Nat. Mater.*, 2013, **12**, 1038–1044.

59 M. Schubert, D. Dolfen, J. Frisch, S. Roland, R. Steyrleuthner, B. Stiller, Z. Chen, U. Scherf, N. Koch, A. Facchetti and D. Neher, *Adv. Energy Mater.*, 2012, **2**, 369–380.

60 J. A. Love, C. M. Proctor, J. Liu, C. J. Takacs, A. Sharenko, T. S. van der Poll, A. J. Heeger, G. C. Bazan and T.-Q. Nguyen, *Adv. Funct. Mater.*, 2013, **23**, 5019–5026.

61 X. Liu, Y. Sun, L. A. Perez, W. Wen, M. F. Toney, A. J. Heeger and G. C. Bazan, *J. Am. Chem. Soc.*, 2012, **134**, 20609–20612.

62 S. Nam, D. S. Chung, J. Jang, S. H. Kim, C. Yang, S.-K. Kwon and C. E. Park, *J. Electrochem. Soc.*, 2010, **157**, H90–H93.

63 W. H. Lee, J. A. Lim, D. H. Kim, J. H. Cho, Y. Jang, Y. H. Kim, J. I. Han and K. Cho, *Adv. Funct. Mater.*, 2008, **18**, 560–565.

64 M. R. Hammond, R. J. Kline, A. A. Herzing, L. J. Richter, D. S. Germack, H.-W. Ro, C. L. Soles, D. A. Fischer, T. Xu, L. Yu, M. F. Toney and D. M. DeLongchamp, *ACS Nano*, 2011, **5**, 8248–8257.

65 R. Kroon, A. Diaz de Zerio Mendaza, S. Himmelberger, J. Bergqvist, O. Backe, G. C. Faria, F. Gao, A. Obaid, W. Zhuang, D. Gedefaw, E. Olsson, O. Inganas, A. Salleo, C. Muller and M. R. Andersson, *J. Am. Chem. Soc.*, 2014, **136**, 11578–11581.